



Pd-WO_x heterostructures immobilized by MOFs-derived carbon cage for formic acid dehydrogenation

Anqi Zhang, Jianhui Xia, Qilu Yao^{*}, Zhang-Hui Lu^{*}

Institute of Advanced Materials, Key Lab of Fluorine and Silicon for Energy Materials and Chemistry of Ministry of Education, College of Chemistry and Chemical Engineering, Jiangxi Normal University, Nanchang 330022, China

ARTICLE INFO

Keywords:

Formic acid
Dehydrogenation
Metal organic frameworks
Heterostructure
Carbon cage

ABSTRACT

Formic acid (FA), a major product formed in biomass processing and CO₂ reduction, has attracted considerable attention as a promising renewable liquid-phase hydrogen carrier. Designing highly efficient catalysts for FA dehydrogenation is a key challenge for fuel cell-based hydrogen economy. Herein, Pd-WO_x nano-heterostructures (2.9 nm in diameter) anchored on ZIF-8 @ZIF-67 core-shell MOFs-derived nitrogen-doped porous carbon cage (NPCC) are fabricated for the first time through a phosphate mediation approach. Strong adsorption and dispersion of Pd²⁺ in the phosphate-modified NPCC are essential for the synthesis of highly dispersed ultrafine Pd nanoparticles. The alkaline solution produced during the subsequent reduction process of metal ions can remove the phosphate. The obtained Pd-WO_x/(P)NPCC catalyst presents an extraordinarily catalytic performance (TOF, 2877 h⁻¹ at 303 K and 6135 h⁻¹ at 323 K) with a 100% H₂ selectivity and conversion toward FA dehydrogenation. The superior performance of Pd-WO_x/(P)NPCC is likely due to the strong interaction effect between Pd-WO_x and NPCC; unique structures of Pd-WO_x nano-heterostructures; and NPCC with hollow and large surface area and abundant surface defects. Kinetic isotope effect (KIE) measurements demonstrated that cleavage of C—H bond is the rate-determining step for HCOOH dehydrogenation. This study provides new insights into a facile and controllable synthesis strategy of inexpensive and efficient catalysts for high-efficiency dehydrogenation of liquid-phase hydrogen carrier.

1. Introduction

Replacement of conventional fossil fuels with a clean CO₂ neutral energy cycle is a key global challenge. Hydrogen is a promising energy carrier that has been largely used in fuel cell-based systems [1]. Safe and efficient storage of hydrogen is an important but challenging issue in obtaining hydrogen-based economy [2]. Liquid hydrogen storage materials have attracted considerable research attention due to their easy recharging and transportation [3,4]. Formic acid (FA, HCOOH), a major product formed in biomass processing and CO₂ reduction, has been increasingly used as a suitable hydrogen storage material because of its renewable property, wide range of sources, high hydrogen content, and ability to remain liquid at room temperature [5–7]. FA can catalytically be decomposed via dehydrogenation (HCOOH → H₂ + CO₂) and dehydration (HCOOH → H₂O + CO) pathways [8,9]. The latter is the unwanted reaction and should be circumvented for the subsequent conversion of hydrogen into electrical energy in fuel cells because it produces CO impurity, which is toxic to fuel cell catalysts.

Various methods for the design and development of suitable catalysts for the dehydrogenation of FA have been recently proposed [10–12]. The development of heterogeneous catalysts may eliminate the disadvantage of homogeneous catalysts, which are difficult to separate from the reaction mixture and the requirement of ligands/additives [13–17]. Recent studies demonstrated that Pd alloyed with noble metal nanoparticles (NPs) present excellent activity in FA dehydrogenation, especially Pd–Au and Pd–Ag NPs catalysts [18–32]. However, high cost and rarity of noble elements considerably hinder their widespread use. Therefore, many approaches for designing catalysts without or with low noble-metal content have been proposed, but the dehydrogenation of FA catalyzed using these catalysts still remains slow and inefficient even under high reaction temperatures [33–36]. Therefore, reducing the content of noble metals and significantly improving their efficiency while maintaining or increasing the catalytic activity of catalysts remain challenging but are urgently necessary [37,38].

Heterointerfaces can induce numerous self-built electric fields at interfaces for fast charge transfer and ion diffusion; therefore, the

^{*} Corresponding authors.

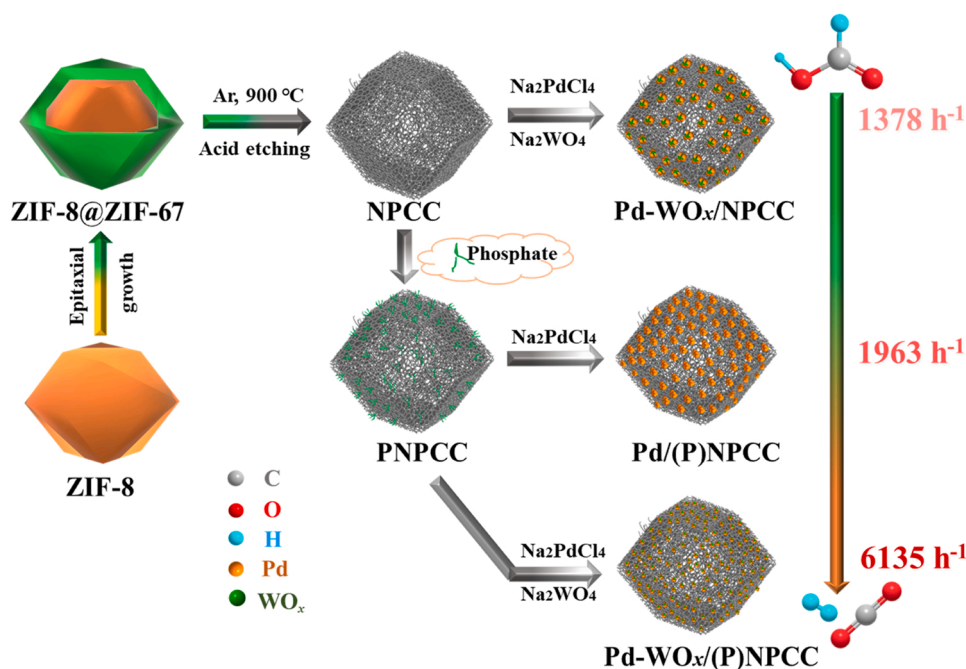
E-mail addresses: yaoqilu@jxnu.edu.cn (Q. Yao), luzh@jxnu.edu.cn (Z.-H. Lu).

<https://doi.org/10.1016/j.apcatb.2022.121278>

Received 20 December 2021; Received in revised form 28 February 2022; Accepted 2 March 2022

Available online 3 March 2022

0926-3373/© 2022 Elsevier B.V. All rights reserved.



Scheme 1. Schematic illustration for the fabrication of Pd-WO_x/(P)NPCC, Pd/(P)NPCC and Pd-WO_x/NPCC NCs.

synthesis of heterogeneous structures is likely effective in improving the reaction efficiency [39]. Tungsten oxide material is a typical n-type semiconductor and often used to construct heterojunctions for photo-[40] and electrocatalytic reactions [41]. In addition, WO_x can be considered a potential catalytic promoter for FA dehydrogenation because of its ability to couple with metals strongly and interact with reactants due to its acid stability and oxygen deficiency [42–44]. Porous carbon is an ideal substrate to stabilize active NPs due to its advantages of large specific surface area, tunable porous structure, and fast electron and efficient mass transfer [45–50]. The modification of the carbon material surface and increase of its porosity are beneficial to the increase of particle adsorption sites and promotion of particle dispersion [51]. Phosphoric acid (H₃PO₄), as a chemical activator, not only modulate the porosity of carbon, but also produces P–O bonds on the carbon surface to promote the dispersion of active metallic NPs and offer them strong interaction sites [52,53]. Active species that cooperate with a catalytic promoter and are immobilized by a versatile matrix may exhibit excellent catalytic activity [54–57].

Herein, we report a novel and facile synthesis of Pd–WO_x nano-heterojunctions immobilized by phosphate-mediated N-doped porous carbon cages (Pd–WO_x/(P)NPCC) as an efficient catalyst for FA dehydrogenation. NPCC is utilized as the substrate by annealing the core-shell structure of zeolite imidazole skeleton ZIF-8 @ZIF-67. Tungsten oxide is introduced as the catalytic accelerator for active species Pd to form Pd–WO_x heterojunctions. Properly dispersed Pd–WO_x nano-heterojunctions with a mean size of 2.9 nm are anchored on the NPCC substrate. The as-synthesized Pd–WO_x/(P)NPCC catalyst exhibits an extraordinarily high catalytic activity for FA dehydrogenation with 100% hydrogen selectivity, 100% conversion, and high initial turnover frequency (TOF) value of up to 2877 h^{−1} at 303 K and 6135 h^{−1} at 323 K.

2. Experimental

2.1. Synthetic procedures

N-doped porous carbon cage (NPCC) was synthesized by direct pyrolysis of the core@shell structure ZIF-8 @ZIF-67. Phosphate-mediated N-doped porous carbon cage (PNPCC) was obtained via hydrothermal method of NPCC with H₃PO₄ at 130 °C for 12 h. Pd–WO_x/(P)NPCC was

fabricated using a conventional wet chemical strategy at ambient conditions. Distilled water (5.0 mL) containing Na₂PdCl₄ (29.42 mg, 0.1 mmol Pd), Na₂WO₄·2 H₂O (6.60 mg, 0.02 mmol W), and PNPCC (60.30 mg) were mixed and then ultrasonically treated for 30 min. NaBH₄ (1 mmol) was then placed into the mixed solution under vigorous magnetic stirring. Precipitates were isolated by centrifugation (10,000 rpm, 5 min) and then washed thoroughly with an excessive amount of water after complete reduction of metal salt. Finally, the Pd–WO_x/(P)NPCC catalyst was obtained as a dark powder. Pd–WO_x/(P)NPCC catalysts with different contents of WO_x and Pd–WO_x loading were also synthesized by changing amounts of Na₂WO₄·2 H₂O and NPCC, respectively, for comparison. Pd–WO_x supported on NPCC, NC₁ derived from ZIF-8, PNC₁ obtained after hydrothermal phosphorylation of NC₁, NC₂ derived from ZIF-67, and PNC₂ obtained after hydrothermal phosphorylation of NC₂ were also prepared using the same method (details are described in the [Supporting Information](#)).

2.2. Hydrogen generation from FA-SF aqueous solution

The catalytic activity of all catalysts for the dehydrogenation of FA in FA-SF aqueous solution was determined via volumetric measurement and the rate of generated gas. Briefly, a mixture of as-prepared catalyst and distilled water (3.0 mL) were placed in a two-necked round-bottomed flask (50 mL). Catalytic reaction started immediately after adding 2.0 mL of the mixed aqueous solution containing FA (2.5 mmol) and sodium formate (SF) with a molar ratio of 1/3. The volume of the generated gas was monitored by recording the displacement of water in the gas burette. The flask was immersed in a water bath to maintain the temperature at design value.

3. Results and discussion

3.1. Fabrication and characterization

The synthesis process of Pd–WO_x/(P)NPCC, Pd/(P)NPCC, and Pd–WO_x/NPCC is illustrated in [Scheme 1](#). First, a core-shell structure of zeolite imidazole skeleton ZIF-8 @ZIF-67 was prepared using seed epitaxial growth method (details are shown in the [Supporting Information](#)) and used as the prototype to fabricate nitrogen-doped porous

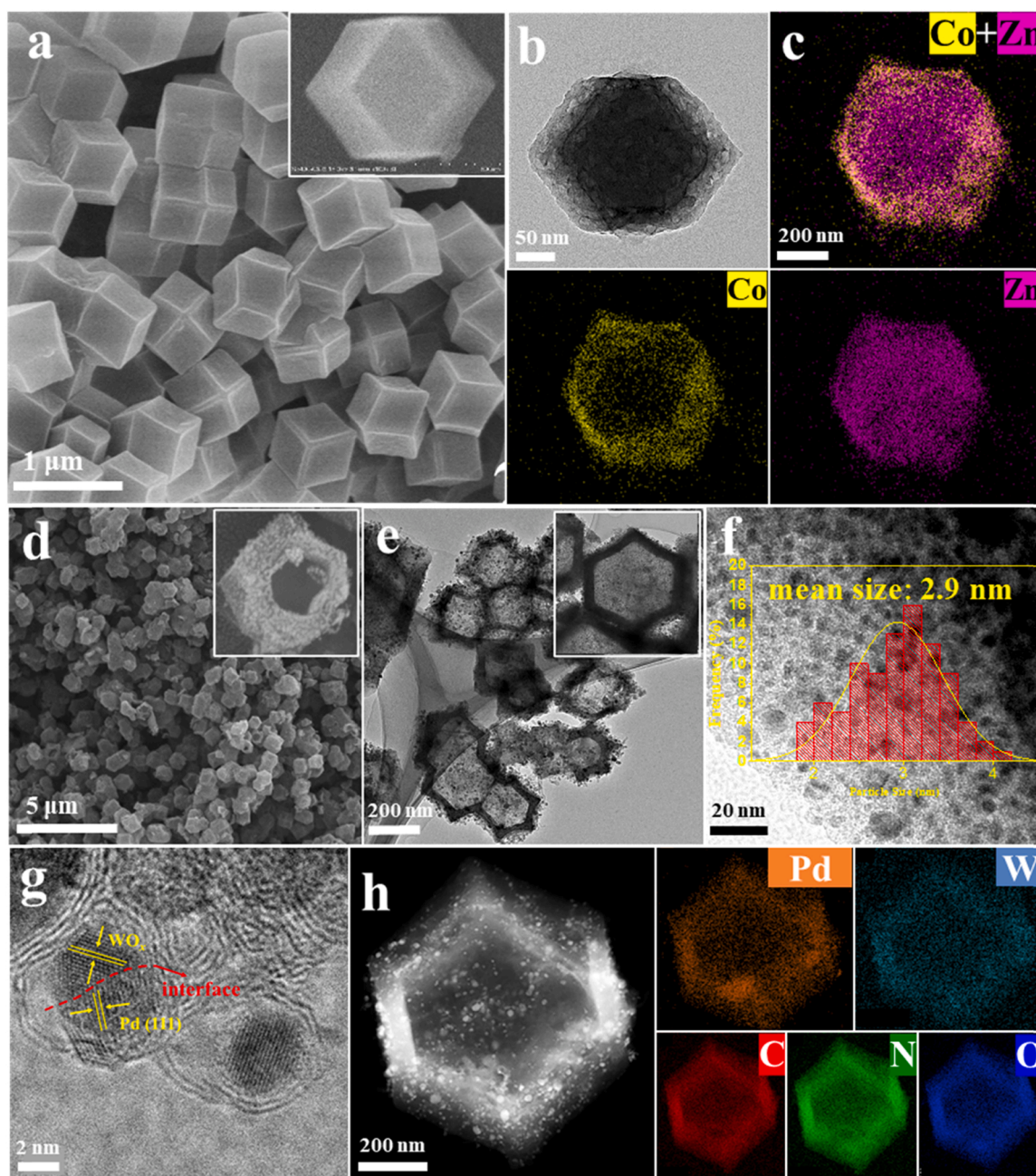


Fig. 1. (a) SEM images, (b) TEM image, and (c) elemental mapping images of ZIF-8 @ZIF-67; (d) SEM images, (e) TEM images, (f) Particle size distribution, (g) HRTEM image, and (h) HAADF-STEM image and EDS elemental mapping images of Pd-WO_x/(P)NPCC NCs.

carbon nanocage (NPCC) via pyrolysis at 900 °C under argon flow. Second, phosphate-mediated nitrogen-doped porous carbon nanocage (PNPCC) were prepared via hydrothermal phosphorylation of NPCC. Finally, Pd-WO_x/(P)NPCC and Pd-WO_x/NPCC catalysts were obtained through the co-reduction of Pd and W precursors with a conventional wet chemical method using PNPCC and NPCC as the carrier, respectively. Pd/(P)NPCC was also prepared using the same method without adding the W precursor for comparison. The phosphate species of PNPCC were removed by the alkaline solution produced during the subsequent reduction process of Pd ions via NaBH₄.

The crystal structure and morphology of as-synthesized ZIF-67, ZIF-8, and ZIF-8 @ZIF-67 were characterized via X-ray diffraction (XRD), scanning electron microscopy (SEM), and transmission electron microscopy (TEM). As shown in Fig. S1, the obtained ZIF-8 @ZIF-67 sample reasonably shares similar characteristics with ZIF-8 and ZIF-67 crystals

in terms of peak intensity and position. SEM and TEM images revealed that all synthesized ZIF-67, ZIF-8 and ZIF-8 @ZIF-67 samples show a well-defined rhombic dodecahedron structure with clear outline, smooth surface, and uniform size distribution (Figs. 1a, b, S2, and S3). Energy-dispersive X-ray spectroscopy (EDS) elemental mapping images display that C and N are uniformly distributed throughout the ZIF-8 @ZIF-67 while Zn and Co are distributed in the center and outside of the sample, respectively (Figs. 1c and S4). This finding further confirms the successful synthesis of the core@shell structure ZIF-8 @ZIF-67. The N-doped porous carbon cage (NPCC) was then fabricated via direct pyrolysis of the properly designed core-shell structure ZIF-8 @ZIF-67. The ZIF-67 shell first decomposed during the pyrolysis process to form a rigid carbon shell due to its low thermal stability and then exerted an outward adhesive force to inhibit inward contraction of ZIF-8 nucleus [62]. An explicit carbon cage (Fig. S5) can be obtained through the

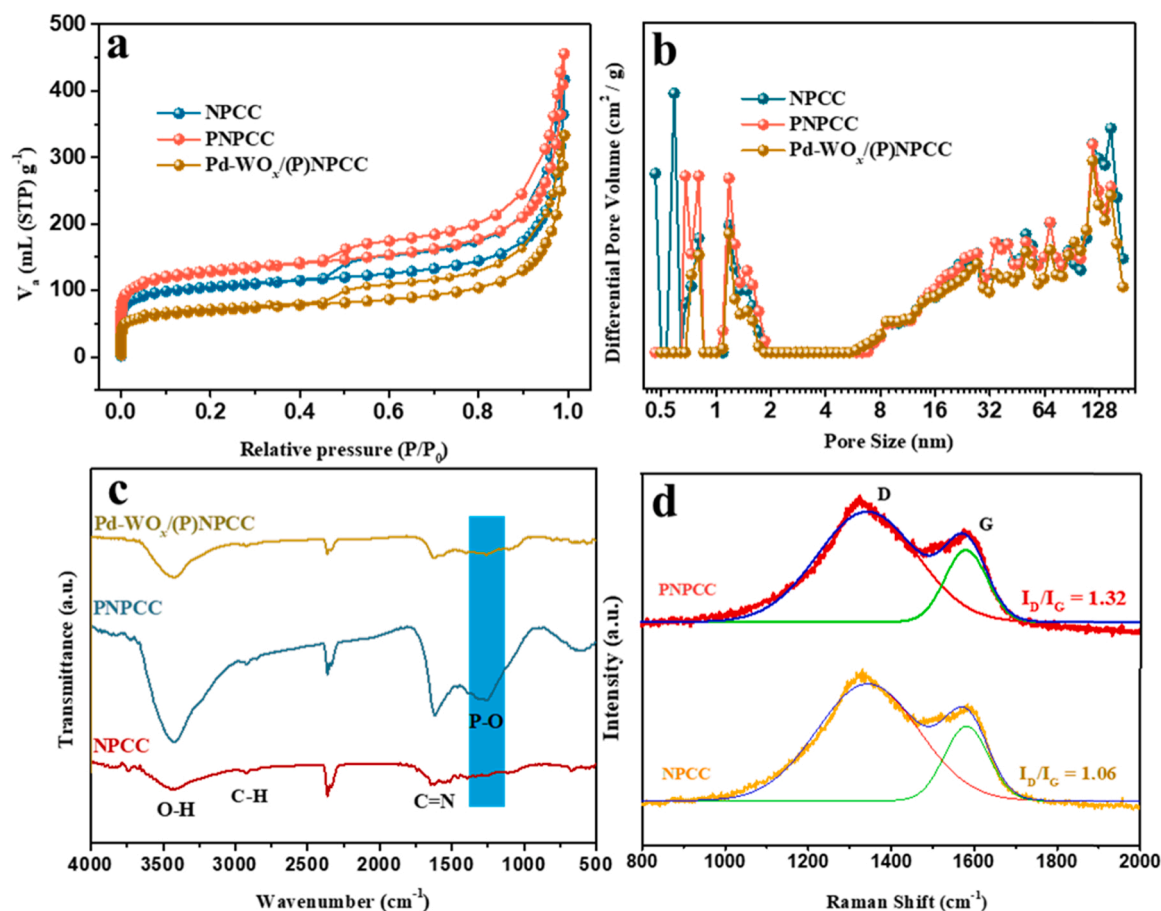


Fig. 2. (a) Nitrogen adsorption-desorption isotherms, (b) corresponding pore distribution curves, (c) FT-IR spectra of NPCC, PNPCC, and Pd-WO_x/(P)NPCC; (d) Raman spectra of the NPCC and PNPCC.

decomposition of the ZIF-8 core, and a large number of grass-like carbon nanotubes (CNTs) were grown on the surface of the carbon cage [58]. The formation of CNTs was mainly due to the catalytic effect of Co NPs derived from the ZIF-67 shell [59], and the in situ generated Co NPs (~14.3 nm) are embedded into several carbon layers (Fig. S6). After acid etching, the residual Zn and Co was reduced from 0.8 wt% and 17.9–0.02 wt% and 1.5 wt% (Table S1a), respectively, whose effect on the activity for FA dehydrogenation can be neglected (vide infra). In contrast, pyrolysis treatment of ZIF-67 or ZIF-8 sole can generate polyhedral carbon structures but fail to produce hollow structures (Fig. S7) under similar heat treatment conditions. As shown in Scheme 1 and Fig. S6a, phosphate-mediated N-doped porous carbon cage (PNPCC) was obtained via hydrothermal method of NPCC with H₃PO₄, which keeps the same hollow polyhedral carbon structure (Fig. 1d and e) as NPCC (Fig. S5). After the introduction of Pd-WO_x to PNPCC, the resulting Pd-WO_x/(P)NPCC still maintains a nanocage-like structure (Fig. 1d and e). As depicted in Fig. 1f, Pd-WO_x NPs with a mean size of ~2.9 nm are highly dispersed on nanocages. Particularly, high-resolution TEM (HR-TEM) observations demonstrate the evident interface coexistence between Pd (111) with a lattice fringe of 0.224 nm and WO_x with a lattice fringe of 0.37 nm [60,61], thereby indicating the formation of Pd-WO_x heterostructures (Figs. 1g and S8). The corresponding EDS mapping image with high resolution can further demonstrate the formation of heterojunction interfaces (Fig. S8). The growth interface denoted by a red line is easily distinguished by the WO_x and Pd (111) plane (Fig. 1g). The corresponding EDS elemental mappings confirm the homogeneous dispersion of Pd, W, Co, C, N, and O (Figs. 1h and S9) in the Pd-WO_x/(P)NPCC sample. Inductively coupled plasma-atomic emission spectroscopy (ICP-AES) analysis showed that the Pd content of

Pd-WO_x/(P)NPCC is 14.3 wt%, which is consistent with the initially designed Pd content. However, the content of W is only 0.7 wt%, much lower than the theoretical W loading (4.9 wt%) (Table S1b), which may be because W is not completely digested in acid during ICP sample preparation. Additionally, the content of phosphate almost can be neglected after the reduction of metal ions in the alkaline solution according to ICP-AES analysis (Table S1b). Hence, the intermediary role of phosphate in promoting the dispersion of metal NPs is confirmed.

As shown in Fig. S10a, Pd-WO_x NPs supported on NPCC without phosphate treatment (denoted Pd-WO_x/NPCC) shows a larger size of 8.1 nm compared with that of Pd-WO_x/(P)NPCC (Fig. 1f). This finding indicated that the strong adsorption ability of phosphate for Pd²⁺ and W⁶⁺ ions can synthesize ultrasmall and highly distributed Pd-WO_x NPs during the preparation process. Similarly, WO_x-free Pd NPs supported by PNPCC (denoted Pd/(P)NPCC) exhibit a large diameter of 7.6 nm (Fig. S10b), thereby implying that the ultrafine particle size of Pd-WO_x/(P)NPCC is caused by not only the phosphate-mediated effect but also the formation of the Pd-WO_x heterointerface. Support-free Pd-WO_x NPs show severe aggregation with a large mean size of 20.7 nm (Fig. S10c). This significant size difference reveals the important role of PNPCC as a novel support for regulating the growth of NPs.

XRD measurements were performed to determine the crystalline structure of Pd-WO_x/(P)NPCC and its comparative samples. As shown in Fig. S11, typical diffraction peaks of Pd (111) (PDF#87-0643) at 40.1° and 46.6° appear in Pd-WO_x/(P)NPCC, Pd-WO_x and Pd/(P)NPCC samples. The XRD pattern of the product shows nearly no characteristic peak of WO_x, which may attribute to their relative low content (Table S1) and small size on the catalyst surface (Fig. 1f). Typical diffraction peaks of amorphous carbon (2θ = 24°) and Co (2θ = 44°),

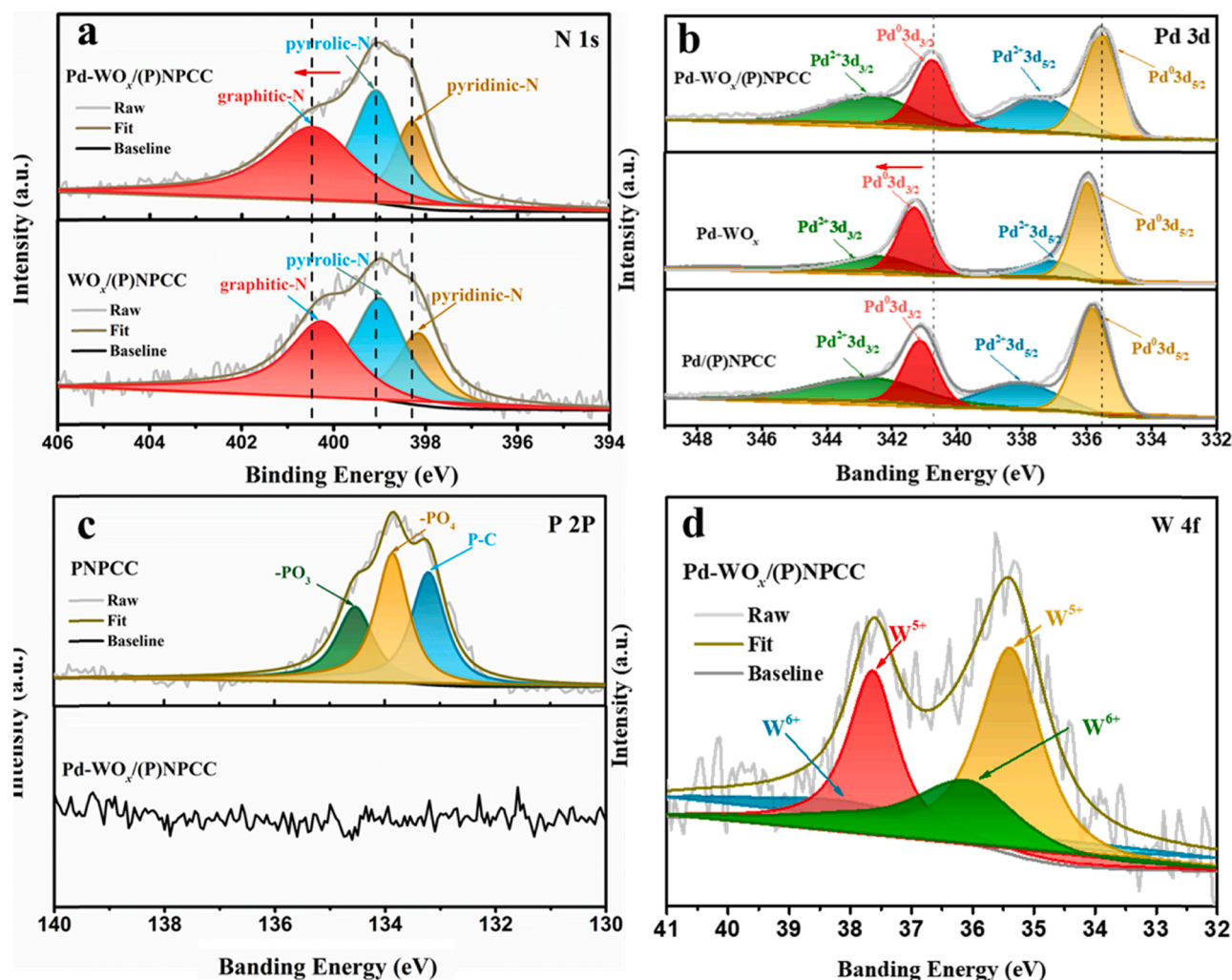


Fig. 3. High resolution XPS spectra of (a) N 1s, (b) Pd 3d, (c) P 2p, and (d) W 4f of the synthesized samples.

PDF#15–0806) are present in all components, except for pure Pd–WO_x NPs.

The N₂ adsorption/desorption isotherm was measured to characterize specific surface area and pore size distribution of synthesized materials. All samples show characteristics of type II isotherms with H4 hysteresis loops (Fig. 2a). The large volume overtakes at P/P₀ = 0 and the evident hysteresis appears at P/P₀ > 0.9, thereby indicating the presence of a highly porous structure. Compared with Brunauer–Emmett–Teller (BET) surface area of ZIF-8-derived NC₁ (266.8 m²·g^{−1}) and ZIF-67-derived NC₂ (95.2 m²·g^{−1}) the core@shell structure ZIF-8 @ZIF-67-derived NPCC shows an increased surface area (391.0 m²·g^{−1}) (Figs. S12 and 2a). Notably, the surface area and pore volume of NPCC increase from 391.0 m²·g^{−1} and 0.50 cm³·g^{−1} to 471.9 m²·g^{−1} and 0.54 cm³·g^{−1} of PNPCC (produced after the hydrothermal phosphorylation of NPCC), respectively (Fig. 2a and b), due to the pore-expanding effect caused by the dehydration and oxidation of phosphoric acid [62]. Compared with PNPCC, the significant decrease of the specific surface area (249.7 m²·g^{−1}) and pore volume (0.43 cm³·g^{−1}) of Pd–WO_x/(P)NPCC revealed that some defects and/or pores are filled with Pd–WO_x NPs (Table S2). Pore size distribution analyses showed that sufficient micropores are present in all samples due to the release of gases and evaporation of Zn from ZIF-8 during pyrolysis as well as phosphoric acid etching during the hydrothermal process (Fig. 2b). The presence of macropores further proves the existence of a hollow structure, consistent with the results of TEM and SEM images (Figs. 1e and S13). The hollow carbon architecture with high porosity can efficiently

facilitate the diffusion of reactants and products in the reaction process to improve the reaction dynamics [50].

Fourier transform infrared spectrometry (FTIR) was used to examine the chemical structure of synthesized materials. As shown in Fig. 2c, aromatic C=N (1647 cm^{−1}), C–H (2922 cm^{−1}), and O–H (3424 cm^{−1}) stretching vibrations can be assigned to dimethylimidazole ligand. Moreover, the presence of P–O stretching vibration (1272 cm^{−1}) in PNPCC obtained after hydrothermal phosphorylation of NPCC indicated that phosphate species are successfully anchored to the surface of NPCC. The disappearance of the vibration band of P–O in Pd–WO_x/(P)NPCC after the reduction of metal ions suggested the removal of phosphate through the alkaline solution produced during the reduction process of metal ions by NaBH₄. ICP–OES analysis demonstrated that the P content decreases from 8.4 wt% of PNPCC to 0.2 wt% of Pd–WO_x/(P)NPCC (Table S1b). This finding further confirmed the removal of phosphate species.

Peaks located at 1325 (D-band) and 1588 (G-band) cm^{−1} in the Raman spectra of NPCC and PNPCC (Fig. 2d) belong to lattice defects or edges and graphitic structure carbon, respectively [63]. The higher intensity ratio (I_D/I_G) of PNPCC (1.32) than that of NPCC (1.06) indicated that the degree of defects or the concentration of defect sites become higher after the hydrothermal phosphorylation treatment of NPCC. The analysis of the hydrothermal process of phosphoric acid demonstrated that phosphoric acid can activate carbon and create holes on the carbon surface. Moreover, a portion of phosphoric acid is transformed into metaphosphoric acid, which attacks defects of NPCC and forms new

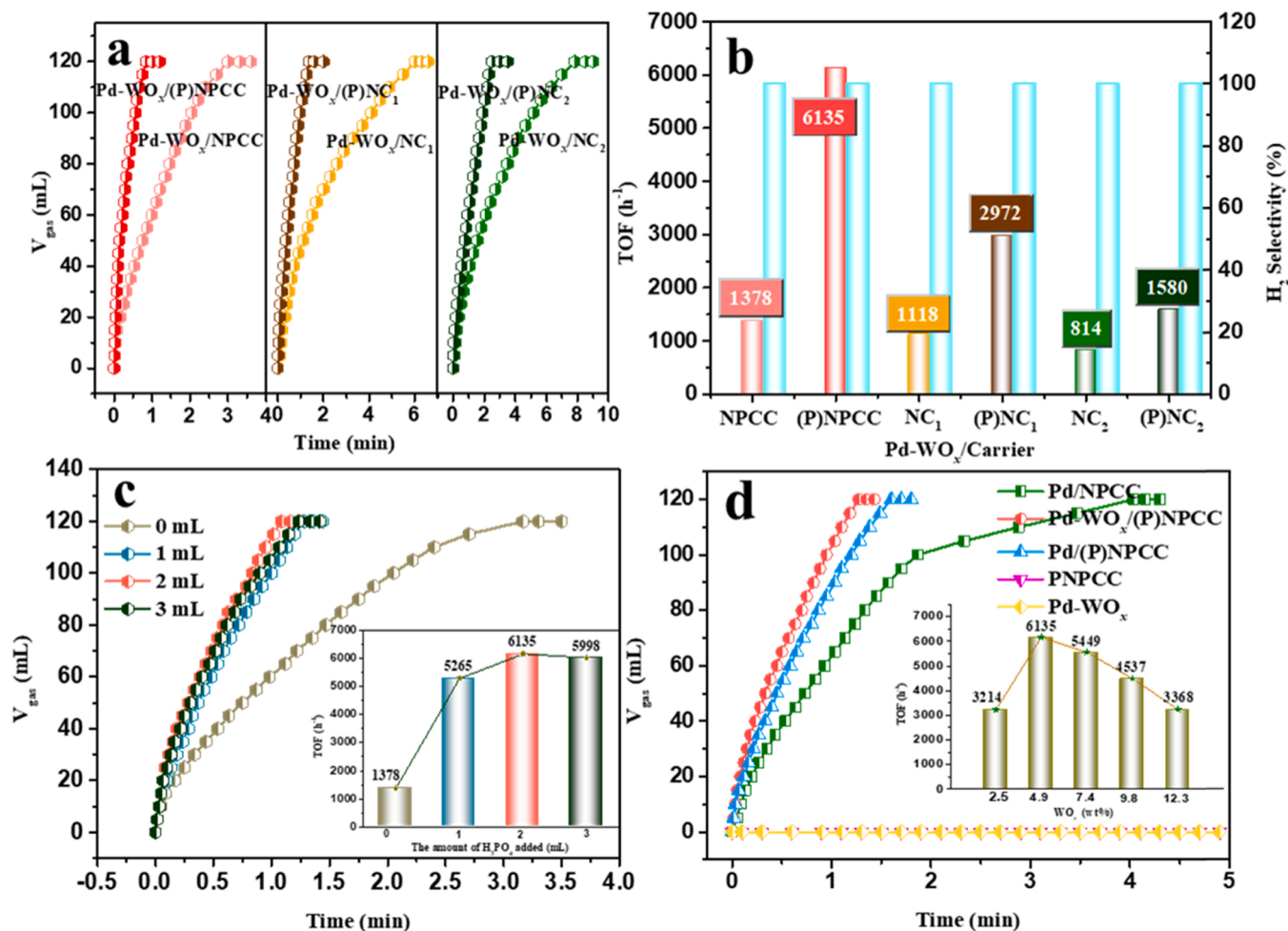


Fig. 4. Generated $V_{(H_2 + CO_2)}$ versus time for the dehydrogenation of FA in FA-SF aqueous solution at 323 K over (a) Pd-WO_x NPs with different supports, (b) the corresponding TOF values, (c) Pd-WO_x NPs with supports doped with different amounts of phosphorus (inset: the corresponding TOF values), and (d) Pd-WO_x(P) NPCC, Pd/(P)NPCC, Pd/NPCC, PNPCC, and Pd-WO_x NCs (inset: the TOF values at different loadings of WO_x) ($n_{FA}/n_{SF} = 1:3$, $n_{Pd}/n_{FA} = 0.04$).

adsorption sites for metal ions [63]. The N-doped porous carbon with additional defects and adsorption sites for metal ions is conducive to the formation of ultrafine metal NPs [64]. Therefore, Pd-WO_x(P)NPCC displays a smaller size of Pd-WO_x NPs than Pd-WO_x/NPCC (vide supra).

X-ray photoelectron spectroscopy (XPS) analyses were performed to investigate chemical states and electronic effects of Pd-WO_x(P)NPCC and its comparative samples. Fig. S14 shows the survey XPS spectrum of Pd-WO_x(P)NPCC, in which signals of Pd, W, O, N, and C can be accurately identified. As shown in Fig. S15, C 1s spectra of Pd-WO_x(P)NPCC with four peaks located at 284.7, 285.6, 287.5, and 290.7 eV can be appropriately fitted to C-C/C=C, C-N, C-O, and O-C=O, respectively [28]. The identification of C-N bonds clarifies the N doping in carbon carriers. Moreover, C 1s peaks of Pd-WO_x(P)NPCC remain nearly unchanged compared with those of WO_x(P)NPCC. As shown in Fig. 3, N 1s spectra of Pd-WO_x(P)NPCC can be deconvoluted into three peaks at binding energies (BEs) of 400.5, 399.1, and 398.3 eV that correspond to graphitic, pyridinic, and pyrrolic N, respectively [65]. N 1s in Pd-WO_x(P)NPCC shifts to higher BEs relative to WO_x(P)NPCC. Meanwhile, BEs of Pd⁰ 3d_{3/2} at 340.8 eV and Pd⁰ 3d_{5/2} at 335.5 eV for Pd-WO_x(P)NPCC shift to a lower value than the free Pd-WO_x (Pd⁰ 3d_{3/2} at 341.3 eV and Pd⁰ 3d_{5/2} at 336 eV) [28]. This finding indicated that a strong metal-support interaction (SMSI) exists between Pd-WO_x and (P)NPCC and electron transfer efficiently occurs from N to Pd-WO_x. In addition, BEs of Pd 3d_{3/2} and 3d_{5/2} negatively shift from 341.1 and 335.8 eV (Pd/(P)NPCC) to 340.8 and 335.5 eV (Pd-WO_x(P)NPCC), respectively, after WO_x addition. This phenomenon demonstrated that

some electrons were transferred from WO_x to Pd at heterostructure interfaces, and the strong internal electron effect formed at the heterostructure interface leads to electron transfer and redistribution [66]. Based on the XPS results, the electronic structure of Pd-WO_x NPs can be regulated not only by the heterogeneous structure formed by Pd and WO_x through the electronic synergistic effect at the heterogeneous interface but also optimized by PNPCC as an electron donor through the SMSI effect. Formate adsorption can be enhanced by donating back from electron-rich Pd to formate due to the formation of a heterogeneous junction and SMSI-derived modification in the electronic structure of Pd [67,68]. This phenomenon can lead to the increase of catalytic activity of FA dehydrogenation.

A distinct P 2p peak can be deconvoluted into three peaks assigned to phosphate (–PO₄, 133.6 eV), metaphosphate (–PO₃, 134.5 eV), and P–C (133.0 eV) bonds in PNPCC (Fig. 3c), thereby confirming the existence of –PO₄ and –PO₃ grafted on the defect of carbon material by P–C bonds [69,70]. Portions of phosphoric acid can be converted to metaphosphoric acid during the hydrothermal process, and both attack defects on the carbon that leave –PO₃ and –PO₄ on the surface [71]. This finding can be further confirmed by XPS spectra of O 1s of carbon materials before and after hydrothermal phosphorylation given that the intensity of the O 1s peak increases sharply after phosphate anchoring (Fig. S16). Additionally, the disappearance of the P signal after the reduction of metal ions is consistent with the results of ICP-AES and FTIR analyses (Figs. 2c and 3c and Table S1b). The high-resolution W 4f spectra can be deconvoluted into two pairs of peaks, corresponding to the binding

energies of W oxidation states, W^{5+} (located at 35.4 and 37.6 eV) and the second doublet W^{6+} (located at 36.1 and 38.3 eV) (Fig. 3d) [72]. The content of W^{5+} can indirectly reflect the concentration of oxygen vacancy, which can act as defects to coordinate with metal atoms and the carbon carrier [73]. Peaks centered at BEs of 533.7 and 531.7 eV in the O 1 s XPS spectrum (Fig. S17) are allocated to oxygen vacancies (O_v) and lattice oxygen (O_L), respectively. Notably, the ratio of integrated peak areas of $O_v/(O_v+O_L)$ was calculated to evaluate the O_v concentration in catalysts. The O_v concentration of Pd- WO_x /(P)NPCC (67%) is relatively larger than that of Pd/(P)NPCC (63%). This finding proves the existence of abundant oxygen vacancies in the WO_x dopant. O_v is a common type of defect in transition metal oxides that can form additional unsaturated coordination sites for Pd NPs and favorable for the adsorption of reaction molecules [74]. These intimate interfaces may further facilitate the electronic interaction between the PNPCC host and Pd NPs.

3.2. Catalytic dehydrogenation of FA

Catalytic activity of as-prepared composites toward the dehydrogenation of FA in the presence of SF ($n_{FA}/n_{SF}=1:3$, $n_{Pd}/n_{FA}=0.4$) is tested in a typical water-filled graduated burette system at 323 K. As shown in Fig. 4a, Pd- WO_x loaded on NPCC (Pd- WO_x /NPCC) demonstrates satisfactory catalytic activity for hydrogen evolution reaction (HER) from FA with a turnover frequency (TOF) of 1378 h^{-1} . Notably, Pd- WO_x NPs supported on the phosphorylated carrier (Pd- WO_x /(P)NPCC) show significantly enhanced catalytic activity (Fig. 4a and b) with a high TOF value of 6135 h^{-1} , which surpasses the majority of Pd-based catalysts (Table S3). The large gap between the activity of Pd- WO_x /NPCC and Pd- WO_x /(P)NPCC reflects the significant effect of introducing phosphate as the mediator on the surface of the carbon material on the catalytic activity. The excellent catalytic performance of Pd- WO_x /(P)NPCC can be due to ultrasmall Pd- WO_x NPs induced by the phosphate mediation strategy. SF is used as an accelerator to enhance the catalytic performance of HER from FA dehydrogenation. The optimal ratio of FA/SF for Pd- WO_x /(P)NPCC is 1/3 (Fig. S18). However, Pd- WO_x /(P)NPCC also exhibits hydrogen selectivity and conversion for FA dehydrogenation of 100% with an initial TOF value of 655 h^{-1} at 323 K in the absence of SF. This finding is comparable to optimal monometallic catalysts for HER from FA under mild conditions (Table S3). The generated gas from FA decomposition catalyzed by Pd- WO_x /(P)NPCC was determined by gas chromatography (GC) to be composed of H_2 and CO_2 without CO (Fig. S19).

As shown in Fig. 4a, Pd- WO_x NPs supported on ZIF-8-derived-NC₁ or ZIF-67-derived-NC₂ showed much lower catalytic activity compared with ZIF-8 @ZIF-67-derived NPCC (Fig. 4b), highlighting the advantages of NPCC with hollow structure as the support for FA dehydrogenation. A similar enhanced catalytic performance is also observed in Pd- WO_x NPs supported on (P)NC₁ and (P)NC₂ (Fig. 4a and b) compared with those on NC₁ and NC₂. This finding confirmed that the phosphate mediation approach is a general and useful strategy for enhancing the catalytic performance. Different phosphate precursors, such as ammonium phosphate monobasic ($NH_4H_2PO_4$), ammonium phosphate dibasic ($(NH_4)_2HPO_4$), hypophosphorus acid (H_3PO_2), and sodium hypophosphite (NaH_2PO_2), were also used in place of H_3PO_4 to prove the influence of phosphate mediation methods further. The designed P content in all these synthesized catalysts was maintained at 0.034 mmol. As expected, all synthesized catalysts showed enhanced catalytic activity compared with Pd- WO_x /NPCC (Fig. S20). This finding further confirmed that the phosphate mediation approach can enhance the catalytic performance of the Pd- WO_x catalyst. Pd- WO_x /(P)NPCC catalysts with different amounts of phosphorus were prepared using the same method to obtain the optimal phosphorus doping amount. As observed in Fig. 4c, the catalytic performances of Pd- WO_x NPs supported on the carriers treated with different dosage of H_3PO_4 were tested. It is found that the activity of Pd- WO_x /(P)NPCC increased with the increase of H_3PO_4 dosage from 0 to 2 mL, but the activity does not

increase when it continued to increase to 3 mL. The ICP results revealed that the amount of P on the carriers increased with increasing the amount of H_3PO_4 (Table S1b). Fig. S21 showed that the particle size of Pd- WO_x NPs loaded on the PNPCC treated with 3 mL H_3PO_4 was almost same as that on the PNPCC treated with 2 mL H_3PO_4 .

Neither the PNPCC carrier nor the support-free Pd- WO_x NPs is inactive in the dehydrogenation of FA (Fig. 4d). However, the Pd- WO_x /(P)NPCC catalyst exhibits superior catalytic performance with hydrogen selectivity and conversion of 100% likely due to the SMSI effect between Pd- WO_x and PNPCC. The effect of W doping on the catalytic activity of FA dehydrogenation was also investigated. The Pd- WO_x /(P)NPCC catalyst exhibits enhanced catalytic performance compared with Pd/(P)NPCC for HER from FA under the same reaction conditions. Doped W is not an active metal, but it acts as a promoter and has a boosting effect on the activity, which can be attributed to the synergistic effect of the formed heterogeneous interfaces between Pd and WO_x [40,75–78]. Combined with the HRTEM and XPS results, oxygen vacancies caused by WO_x and the heterogeneous structure formed by Pd and WO_x (Figs. 1g, 3b, S8, and S17) allow the active metal Pd to be in an electron-rich state to increase the catalytic activity for FA dehydrogenation effectively. Moreover, the catalytic activity of Pd/NPCC was lower than those of Pd/(P)NPCC, further confirmed the positive effect of phosphate mediation approach. Additional experiments showed that the optimum loading of WO_x and Pd is 4.9 (inset of Figs. 4d) and 14.3 (Fig. S22) wt%, respectively. In addition, the effect of different pyrolysis temperatures (700–1000 °C) for the synthesis of NPCC on the catalytic activity was also explored (Fig. S23). The optimal calcination temperature is 900 °C. As shown in Fig. S24, CrO_x can enhance the activity similar as that of WO_x , while MoO_x did not show an obvious improvement. Among them, the Pd- WO_x /(P)NPCC NC show the highest catalytic activity.

In addition, the effect of the residual Zn and Co on the reactivity was explored. As shown in Figs. 4d and S22, both WO_x /(P)NPCC and PNPCC have no catalytic activity, indicating that the residual Co in the carrier NPCC is inactive. The catalytic performance of Pd- WO_x NPs supported on (P)NPCC before (Zn: 0.8 wt%, Co: 17.9 wt%, Table S1a) and after acid etching (Zn: 0.02 wt%, Co: 1.5 wt%) were carried out, and it was found that there was little difference in performance (Fig. S25), indicating that Zn and Co cannot contribute to the catalytic property. The ZIF-8 @ZIF-8-derived Co-free NPCC was designed for comparison, because the residual Co NPs in ZIF-8 @ZIF-67-derived NPCC could not be completely removed by acid etching due to the encapsulation of the carbon layer. The ZIF-8 @ZIF-8-derived Co-free NPCC also shows a hollow structure without CNTs (Fig. S26) after pyrolysis treatment. As shown in Fig. S27, there is no difference between the initial TOF values of the Pd- WO_x /(P)NPCC (6135 h^{-1}) and Pd- WO_x /ZIF-8 @ZIF-8-(P)NPCC (6135 h^{-1}). However, the reaction time for the complete FA dehydrogenation catalyzed by Pd- WO_x /(P)NPCC (1.2 min) is slightly faster than that of Pd- WO_x /ZIF-8 @ZIF-8-(P)NPCC (1.3 min). The slightly improved performance may be due to the unique structure of NPCC with CNTs derived from ZIF-8 @ZIF-67, as CNTs can be formed under the catalysis of Co from ZIF-67. Although CNTs do not contribute directly to activity, they have the advantage of reinforcing the 3D hierarchical pore structure and increasing specific surface area (Table S2), thus facilitating fast diffusion of the reactants for catalysis, which is beneficial for catalytic performance. XPS measurements were carried out on the electronic states of Pd and Co in these two catalysts (Fig. S28). Although there is no direct contact between Co and Pd, the slight shifts of the BEs indicate that there is a small interaction between Co and Pd through carbon layers. XRD results showed that no alloy was formed between Co and Pd (Fig. S11). The above results indicate that although there is a small interaction between Co and Pd, its effect on the catalyst performance can be neglected.

Kinetic studies for FA dehydrogenation reaction over Pd- WO_x /(P)NPCC are carried out and presented in Fig. S29. As expected, the H_2 generation rate of the decomposition increases with increasing the concentration of Pd. The plots based on the H_2 generation rate versus

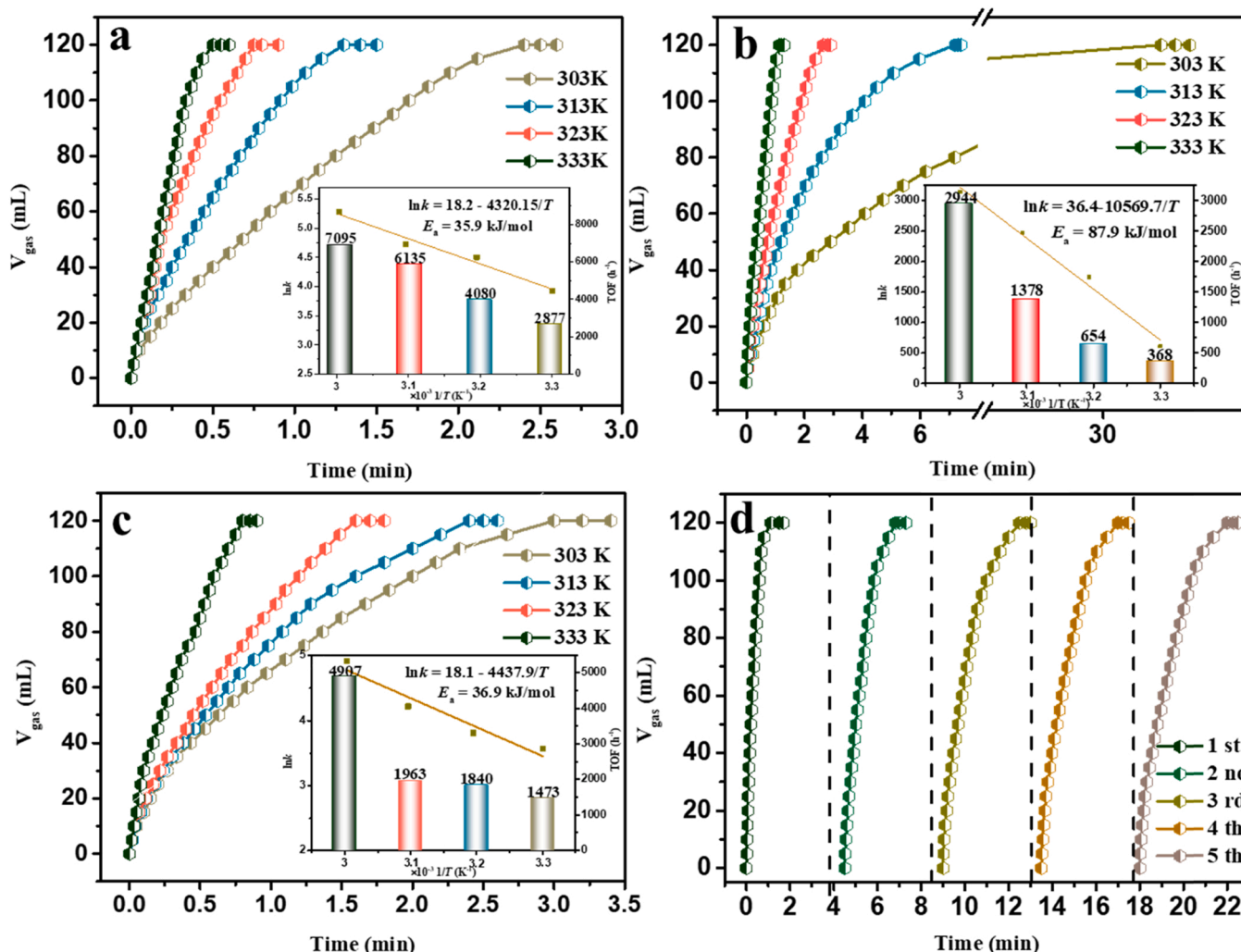


Fig. 5. Generated $V_{\text{H}_2 + \text{CO}_2}$ versus time for the dehydrogenation of FA in FA-SF aqueous solution over (a) Pd-WO_x/(P)NPCC, (b) Pd-WO_x/NPCC, and (c) Pd/(P)NPCC at different temperatures (inset: Arrhenius plot and corresponding TOF values); (d) Stability of the optimized Pd-WO_x/(P)NPCC catalyst for FA dehydrogenation in a FA-SF solution at 323 K ($n_{\text{FA}}/n_{\text{SF}} = 1:3$, $n_{\text{Pd}}/n_{\text{FA}} = 0.04$).

catalyst concentrations (both in logarithmic scale) show a straight line with a slope of 1.32, implying that the FA dehydrogenation reaction is a nearly first-order reaction with respect to the catalyst concentration. The corresponding apparent activation energy (E_a) of Pd-WO_x/(P)NPCC, Pd-WO_x/NPCC, and Pd/(P)NPCC was measured for the dehydrogenation of FA under different temperatures ranging from 303 K to 333 K to understand the effect of the phosphate mediation approach and tungsten oxide addition further (Fig. 5). The results showed that hydrogen generation rates of these catalysts increase by increasing the reaction temperature as expected. As shown in Fig. 5a, E_a of Pd-WO_x/(P)NPCC is calculated at 35.9 kJ·mol⁻¹ according to the Arrhenius equation and clearly lower than that of Pd-WO_x/NPCC at 87.9 kJ·mol⁻¹ (Fig. 5b) and Pd/(P)NPCC at 36.9 kJ·mol⁻¹ (Fig. 5c). This finding demonstrated that the combined effect of phosphate mediator and tungsten oxide doping can significantly reduce the reaction activation energy of FA dehydrogenation. The activation energy of Pd-WO_x/(P)NPCC is also lower than most of the reported values for the same reaction (Table S3), thereby implying the kinetic superiority of the Pd-WO_x/(P)NPCC catalyst for FA dehydrogenation. Notably, the mediation of phosphate leads to a substantial reduction of the activation energy and significantly enhanced catalytic activity (Fig. 4a), due to the ultrafine and highly distributed Pd-WO_x NPs induced by massive defects and interaction sites created by phosphoric acid on the surface of the carbon material during the hydrothermal process, which can be speculated based on the TEM, BET,

and Raman characterization results (vide supra). Previous reports showed that defects can directly serve as molecule activation and adsorption sites for catalysis, thus enhancing catalytic activity and selectivity [70,71].

Reusability tests of the Pd-WO_x/(P)NPCC catalyst for FA dehydrogenation at 323 K are illustrated in Fig. 5d. Complete hydrogen selectivity and conversion can be maintained properly during the test although the hydrogen generation decreases slightly, thereby indicating the acceptable stability of the Pd-WO_x/(P)NPCC catalyst. SEM (Fig. S30a), TEM (Fig. S30b), and XRD (Fig. S31) analyses were performed to characterize the catalyst recovered after the reusability test. Significant changes in the particle size and morphology of the Pd-WO_x/(P)NPCC catalyst were absent after the reusability test. This finding further confirms the excellent stability of the Pd-WO_x/(P)NPCC catalyst for HER from FA dehydrogenation under the present conditions. As shown in Table S1b, the Pd content of Pd-WO_x/(P)NPCC after five cycles was determined at 14.1 wt%, which is slightly lower than the initial Pd content of 14.3 wt%. As a result, the slight prolongation of the reaction time after five cycles is mainly due to the small loss of Pd in the recovery process.

Kinetic isotope effect (KIE) in HER over Pd-WO_x/(P)NPCC was assessed to explore the reaction mechanism in HER from the selective decomposition of HCOOH. H in the -COOH group of HCOOH can be exchanged with D₂O, but the H atom in the -CH group cannot be

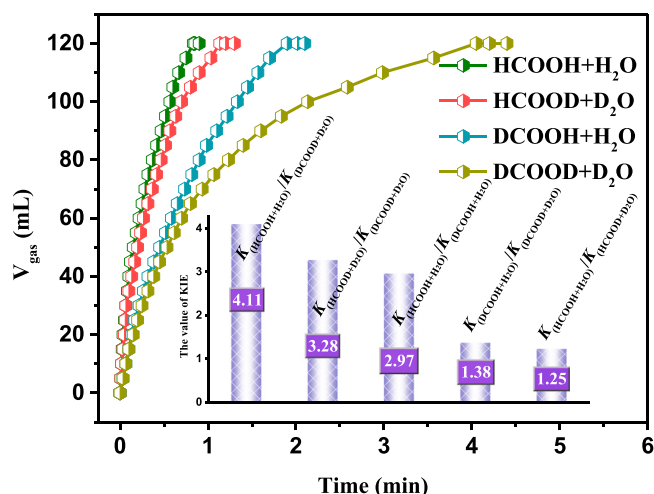


Fig. 6. Isotope-labeled experiments for dehydrogenation of FA over Pd-WO_x/(P)NPCC.

exchanged with D₂O at room temperature [79,80]. Therefore, different reaction substrates, such as HCOOH, formic acid-d₂ (DCOOD), formic acid-d (HCOOD), and formic-d acid (DCOOH), as well as solvents (H₂O and D₂O) were used to carry out the KIE investigation. As shown in Fig. 6, a series of experiments, including HCOOH+H₂O, DCOOD+D₂O, HCOOD+D₂O, and DCOOH+H₂O, was implemented. Initial hydrogen generation rate (*k*) is applied to KIE investigations because the hydrogen generation speed remains nearly unchanged at the initial reaction stage. Values of $k_{(\text{HCOOH}+\text{H}_2\text{O})}/k_{(\text{DCOOD}+\text{D}_2\text{O})}$, $k_{(\text{HCOOD}+\text{D}_2\text{O})}/k_{(\text{DCOOD}+\text{D}_2\text{O})}$, $k_{(\text{HCOOH}+\text{H}_2\text{O})}/k_{(\text{DCOOH}+\text{H}_2\text{O})}$, $k_{(\text{DCOOH}+\text{H}_2\text{O})}/k_{(\text{DCOOD}+\text{D}_2\text{O})}$ and $k_{(\text{HCOOH}+\text{H}_2\text{O})}/k_{(\text{HCOOD}+\text{D}_2\text{O})}$, were 4.11, 3.28, 2.97, 1.38, and 1.25, respectively (Fig. 6). A $k_{\text{H}}/k_{\text{D}}$ value of more than ~1.5 generally indicates a first-order KIE. The obtained results of D labeling experiments showed a first-order KIE in the breaking of H/DCOO* to produce COO* in the presence of Pd-WO_x/(P)NPCC, thereby suggesting a rate-determining step in the dissociation of C–H in the dehydrogenation of HCOOH.

4. Conclusions

Novel Pd-WO_x nano-heterojunctions were successfully anchored on phosphate-mediated N-doped porous carbon cages (Pd-WO_x/(P)NPCC) using a green and facile strategy without surfactant. N-doped porous carbon cages were fabricated through the direct pyrolysis of the appropriately designed core-shell structure ZIF-8@ZIF-67. The as-obtained Pd-WO_x/(P)NPCC catalyst exhibits unexpected catalytic performance for FA dehydrogenation with a high TOF value of 6135 h⁻¹ at 323 K and a low activation energy of 35.9 kJ mol⁻¹. These findings are comparable to those of reported catalysts under the same conditions. The excellent catalytic performance of Pd-WO_x/(P)NPCC can be attributed to the unique structure of Pd-WO_x nano-heterostructures, strong interaction effect between Pd-WO_x and NPCC, and excellent mass transfer efficiency of NPCC with hollow, large surface area, and abundant surface defects. This novel synthesis and highly effective Pd-based nano-heterojunction catalyst supported by MOF-derived N-doped carbon cage provides not only new approaches for the effective application of formic acid as a promising renewable liquid-phase hydrogen carrier for fuel cell applications but also facilitates the fabrication and modification of MOF-derived composites for various applications.

CRediT authorship contribution statement

Anqi Zhang: Conceptualization, Investigation, Formal analysis,

Writing – original draft. Jianhui Xia: Formal analysis. Qilu Yao: Writing – review & editing. Zhang-Hui Lu: Conceptualization, Writing – review & editing, Validation, Funding acquisition, Supervision, Resources.

Declaration of Competing Interest

The authors declare that they have no known competing financial interests or personal relationships that could have appeared to influence the work reported in this paper.

Acknowledgements

The authors wish to acknowledge financial support from the National Natural Science Foundation of China (Nos. 22162014, 22162013, 21763012, and 21802056), Natural Science Foundation of Jiangxi Province of China (No. 20212ACB204009), Sponsored Program for Academic and Technical Leaders of Major Disciplines of Jiangxi Province of China (No. 20212BCJL23059), Sponsored Program for Cultivating Youths of Outstanding Ability in Jiangxi Normal University of China, and Scientific Research Foundation of Graduate School of Jiangxi Province of China (No. YJS2020020).

Appendix A. Supporting information

Supplementary data associated with this article can be found in the online version at doi:10.1016/j.apcatb.2022.121278.

References

- [1] A. Boddien, D. Mellmann, F. Gartner, R. Jackstell, H. Junge, P.J. Dyson, G. Laurenczy, R. Ludwig, M. Beller, Efficient dehydrogenation of formic acid using an iron catalyst, *Science* 333 (2011) 1733–1736.
- [2] Z.K. Zheng, T. Tachikawa, T. Majima, Plasmon-enhanced formic acid dehydrogenation using anisotropic Pd–Au nanorods studied at the single-particle level, *J. Am. Chem. Soc.* 137 (2015) 948–957.
- [3] M. Yadava, Q. Xu, Liquid-phase chemical hydrogen storage materials, *Energy Environ. Sci.* 5 (2012) 9698–9725.
- [4] Q.Y. Bi, X.L. Du, Y.M. Liu, Y. Cao, H.Y. He, K.N. Fan, Efficient subnanometric gold-catalyzed hydrogen generation via formic acid decomposition under ambient conditions, *J. Am. Chem. Soc.* 134 (2012) 8926–8933.
- [5] X.J. Gu, Z.-H. Lu, H.-L. Jiang, T. Akita, Q. Xu, Synergistic catalysis of metal-organic framework-immobilized Au–Pd nanoparticles in dehydrogenation of formic acid for chemical hydrogen storage, *J. Am. Chem. Soc.* 133 (2011) 11822–11825.
- [6] M. Gräsemann, G. Laurenczy, Formic acid as a hydrogen source – recent developments and future trends, *Energy Environ. Sci.* 5 (2012) 8171–8181.
- [7] S. Zhang, Ö. Metin, D. Su, S.H. Sun, Monodisperse AgPd alloy nanoparticles and their superior catalysis for the dehydrogenation of formic acid, *Angew. Chem. Int. Ed.* 52 (2013) 3681–3684.
- [8] K. Mori, M. Dojo, H. Yamashita, Pd and Pd–Ag nanoparticles within a macroreticular basic resin: an efficient catalyst for hydrogen production from formic acid decomposition, *ACS Catal.* 3 (2013) 1114–1119.
- [9] X. Li, A.E. Surkus, J. Rabeah, M. Anwar, S. Dastgier, H. Junge, A. Brückner, M. Beller, Cobalt single-atom catalysts with high stability for selective dehydrogenation of formic acid, *Angew. Chem. Int. Ed.* 59 (2020) 15849–15854.
- [10] Y. Chen, Q.L. Zhu, N. Tsumori, Q. Xu, Immobilizing highly catalytically active noble metal nanoparticles on reduced graphene oxide: a non-noble metal sacrificial approach, *J. Am. Chem. Soc.* 137 (2015) 106–109.
- [11] W.Y. Yu, G.M. Mullen, D.W. Flaherty, C.B. Mullins, Selective hydrogen production from formic acid decomposition on Pd–Au bimetallic surfaces, *J. Am. Chem. Soc.* 136 (2014) 11070–11078.
- [12] H.M. Dai, B.Q. Xia, L. Wen, C. Du, J. Su, W. Luo, G.Z. Cheng, Synergistic catalysis of AgPd@ZIF-8 on dehydrogenation of formic acid, *Appl. Catal. B* 165 (2015) 57–62.
- [13] D. Mellmann, P. Sponholz, H. Junge, M. Beller, Formic acid as a hydrogen storage material – development of homogeneous catalysts for selective hydrogen release, *Chem. Soc. Rev.* 45 (2016) 3954–3988.
- [14] K. Sordakis, C.H. Tang, L. Vogt, H. Junge, P.J. Dyson, M. Beller, G. Laurenczy, Homogeneous catalysis for sustainable hydrogen storage in formic acid and alcohols, *Chem. Rev.* 118 (2018) 372–433.
- [15] Z.P. Li, Q. Xu, Metal-nanoparticle-catalyzed hydrogen generation from formic acid, *Acc. Chem. Res.* 50 (2017) 1449–1458.
- [16] H. Zhong, M. Iguchi, M. Chatterjee, Y. Himeda, Q. Xu, H. Kawanami, Formic acid-based liquid organic hydrogen carrier system with heterogeneous catalysts, *Adv. Sustain. Syst.* 2 (2018), 1700161.

- [17] E. Doustkhah, M. Hasani, Y. Ide, M.H.N. Assadi, Pd nanoalloys for H₂ generation from formic acid, *ACS Appl. Nano Mater.* 3 (2020) 22–43.
- [18] H. Liu, X.Y. Liu, W.W. Yang, M.Q. Shen, S. Geng, C. Yu, B. Shen, Y.S. Yu, Photocatalytic dehydrogenation of formic acid promoted by a superior PdAg@C₃N₄ Mott–Schottky heterojunction, *J. Mater. Chem. A* 7 (2019) 2022–2026.
- [19] K. Tedsree, T. Li, S. Jones, C.W.A. Chan, K.M.K. Yu, P.A.J. Bagot, E.A. Marquis, G. D.W. Smith, S.C.E. Tsang, Hydrogen production from formic acid decomposition at room temperature using a Ag–Pd core–shell nanocatalyst, *Nat. Nanotechnol.* 6 (2011) 302–307.
- [20] S. Masuda, K. Mori, Y. Futamura, H. Yamashita, PdAg nanoparticles supported on functionalized mesoporous carbon: promotional effect of surface amine groups in reversible hydrogen delivery/storage mediated by formic acid/CO₂, *ACS Catal.* 8 (2018) 2277–2285.
- [21] H. Liu, Y. Guo, Y.S. Yu, W.W. Yang, M.Q. Shen, X.Y. Liu, S. Geng, J.R. Li, C. Yu, Z. Y. Yin, H.B. Li, Surface Pd-rich PdAg nanowires as highly efficient catalysts for dehydrogenation of formic acid and subsequent hydrogenation of adiponitrile, *J. Mater. Chem. A* 6 (2018) 17323–17328.
- [22] B.S. Choi, J. Song, M.J. Song, B.S. Goo, Y.W. Lee, Y. Kim, H. Yang, S.W. Han, Core–Shell engineering of Pd–Ag bimetallic catalysts for efficient hydrogen production from formic acid decomposition, *ACS Catal.* 9 (2019) 819–826.
- [23] F.Z. Song, Q.L. Zhu, X.C. Yang, W.W. Zhan, P. Pachfule, N. Tsumori, Q. Xu, Metal–organic framework templated porous carbon-metal oxide/reduced graphene oxide as superior support of bimetallic nanoparticles for efficient hydrogen generation from formic acid, *Adv. Energy Mater.* 8 (2018), 1701416.
- [24] Z.J. Zhang, Y.X. Luo, S.W. Liu, Q.L. Yao, S.J. Qing, Z.H. Lu, A PdAg-CeO₂ nanocomposite anchored on mesoporous carbon: a highly efficient catalyst for hydrogen production from formic acid at room temperature, *J. Mater. Chem. A* 7 (2019) 21438–21446.
- [25] J.W. Hong, D.H. Kim, Y.W. Lee, M.J. Kim, S.W. Kang, S.W. Han, Atomic-distribution-dependent electrocatalytic activity of Au–Pd bimetallic nanocrystals, *Angew. Chem. Int. Ed.* 50 (2011) 8876–8880.
- [26] H. Liu, B. Huang, J. Zhou, K. Wang, Y.S. Yu, W.W. Yang, S.J. Guo, Enhanced electron transfer and light absorption on imino polymer capped PdAg nanowire networks for efficient room-temperature dehydrogenation of formic acid, *J. Mater. Chem. A* 6 (2018) 1979–1984.
- [27] W.H. Wang, T. He, X.H. Liu, W. He, H.J. Cong, Y.B. Shen, L.M. Yan, X.T. Zhang, J. P. Zhang, X.C. Zhou, Highly active carbon supported Pd–Ag nanofacets catalysts for hydrogen production from HCOOH, *ACS Appl. Mater. Interfaces* 8 (2016) 20839–20848.
- [28] S.J. Li, Y.T. Zhou, X. Kang, D.X. Liu, L. Gu, Q.H. Zhang, J.M. Yan, Q. Jiang, A simple and effective principle for a rational design of heterogeneous catalysts for dehydrogenation of formic acid, *Adv. Mater.* 31 (2019), 1806781.
- [29] J. Chen, X.J. Gu, P.L. Liu, H. Zhang, L.L. Ma, H.Q. Su, Achieving efficient room-temperature catalytic H₂ evolution from formic acid through atomically controlling the chemical environment of bimetallic nanoparticles immobilized by isorectular amine-functionalized metal–organic frameworks, *Appl. Catal. B* 218 (2017) 460–469.
- [30] Y. Karatas, A. Bulut, M. Yurderi, I.E. Ertas, O. Alal, M. Gulcan, M. Celebi, H. Kivrak, M. Kaya, M. Zahmakiran, PdAu–MnO_x nanoparticles supported on amine-functionalized SiO₂ for the room temperature dehydrogenation of formic acid in the absence of additives, *Appl. Catal. B* 180 (2016) 586–595.
- [31] Y.J. Huang, X.C. Zhou, M. Yin, C.P. Liu, W. Xing, Novel PdAu@Au/C Core–Shell catalyst: superior activity and selectivity in formic acid decomposition for hydrogen generation, *Chem. Mater.* 22 (2010) 5122–5128.
- [32] Ö. Metin, X.L. Sun, S.H. Sun, Monodisperse gold–palladium alloy nanoparticles and their composition-controlled catalysis in formic acid dehydrogenation under mild conditions, *Nanoscale* 5 (2013) 910–912.
- [33] J.M. Yan, S.J. Li, S.S. Yi, B.R. Wulan, W.T. Zheng, Q. Jiang, Anchoring and upgrading ultrafine NiPd on room-temperature-synthesized bifunctional NH₂-N-rGO toward low-cost and highly efficient catalysts for selective formic acid dehydrogenation, *Adv. Mater.* 30 (2018), 1703038.
- [34] K. Mori, H. Tanaka, M. Dojo, K. Yoshizawa, H. Yamashita, Synergic catalysis of PdCu alloy nanoparticles within a macroreticular basic resin for hydrogen production from formic acid, *Chem. Eur. J.* 21 (2015) 12085–12092.
- [35] Y.L. Qin, J. Wang, F.Z. Meng, L.M. Wang, X.B. Zhang, Efficient PdNi and PdNi@Pd-catalyzed hydrogen generation via formic acid decomposition at room temperature, *Chem. Commun.* 49 (2013) 10028–10030.
- [36] Q.M. Sun, B. Chen, N. Wang, Q. He, A. Chang, C.M. Yang, H. Asakura, T. Tanaka, M.J. Hülsey, C.H. Wang, J.H. Yu, N. Yan, Zeolite-encaged Pd–Mn nanocatalysts for CO₂ hydrogenation and formic acid dehydrogenation, *Angew. Chem. Int. Ed.* 59 (2020) 20183–20191.
- [37] Y.X. Luo, W.D. Nie, Y.Y. Ding, Q.L. Yao, G. Feng, Z.H. Lu, Robust hydrogen production from additive-free formic acid via mesoporous silica-confined Pd-ZrO₂ nanoparticles at room temperature, *ACS Appl. Energy Mater.* 4 (2021) 4945–4954.
- [38] M.L. Huang, Q.L. Yao, G. Feng, Z.H. Lu, Nickel–ceria nanowires embedded in microporous silica: controllable synthesis, formation mechanism, and catalytic applications, *Inorg. Chem.* 59 (2020) 5781–5790.
- [39] F.Y. Zeng, M.H. Yu, W.T. Cheng, W.X. He, Y. Pan, Y.H. Qu, C.L. Yuan, Tunable surface selenization on MoO₂-based carbon substrate for notably enhanced sodium-ion storage properties, *Small* 16 (2020), 2001905.
- [40] M. Jourshabani, S.H. Yun, M.R. Asrami, B.K. Lee, Superior photodegradation of organic compounds and H₂O₂ production over tungsten oxide/carbon nitride heterojunction with sizable heptazine units: dual polycondensation and interface engineering, *Chem. Eng. J.* 427 (2022), 131710.
- [41] W.J. Li, P.M. Da, Y.Y. Zhang, Y.C. Wang, X. Lin, X.G. Gong, G.F. Zheng, WO₃ nanoflakes for enhanced photoelectrochemical conversion, *ACS Nano* 8 (2014) 11770–11777.
- [42] Q.X. Mi, A. Zhanidarova, B.S. Bruntschwig, H.B. Gray, N.S. Lewis, A quantitative assessment of the competition between water and anion oxidation at WO₃ photoanodes in acidic aqueous electrolytes, *Energy Environ. Sci.* 5 (2012) 5694–5700.
- [43] C. Yu, X.F. Guo, Z. Xi, M. Muzzio, Z.Y. Yin, B. Shen, J.R. Li, C.T. Seto, S.H. Sun, AgPd nanoparticles deposited on WO_{2.72} nanorods as an efficient catalyst for one-pot conversion of nitrophenol/nitroacetophenone into benzoxazole/quinazoline, *J. Am. Chem. Soc.* 139 (2017) 5712–5715.
- [44] Y. Chao, X.F. Guo, B. Shen, Z. Xi, Q. Li, Z.Y. Yin, H. Liu, M. Muzzio, M.Q. Shen, J. R. Li, C.T. Seto, S.H. Sun, One-pot formic acid dehydrogenation and synthesis of benzene-fused heterocycles over reusable AgPd/WO_{2.72} nanocatalyst, *J. Mater. Chem. A* 6 (2018) 23766–23772.
- [45] S.H. Liu, Z.Y. Wang, S. Zhou, F.J. Yu, M.Z. Yu, C.Y. Chiang, W.Z. Zhou, J.J. Zhao, J. S. Qiu, Metal–organic-framework-derived hybrid carbon nanocages as a bifunctional electrocatalyst for oxygen reduction and evolution, *Adv. Mater.* 29 (2017), 1700874.
- [46] Y. Pan, K. Sun, S. Liu, X. Cao, K.L. Wu, W.C. Cheong, Z. Chen, Y. Wang, Y. Li, Y. Q. Liu, D.S. Wang, Q. Peng, C. Chen, Y.D. Li, Core-shell ZIF-8@ZIF-67-derived CoP nanoparticle-embedded N-doped carbon nanotube hollow polyhedron for efficient overall water splitting, *J. Am. Chem. Soc.* 140 (2018) 2610–2618.
- [47] C.C. Hou, L. Zou, Q. Xu, A hydrangea-like superstructure of open carbon cages with hierarchical porosity and highly active metal sites, *Adv. Mater.* 31 (2019), 1904689.
- [48] Y.Z. Chen, C.M. Wang, Z.Y. Wu, Y.J. Xiong, Q. Xu, S.H. Yu, H.L. Jiang, From bimetallic metal–organic framework to porous carbon: high surface area and multicomponent active dopants for excellent electrocatalysis, *Adv. Mater.* 27 (2015) 5010–5016.
- [49] H.R. Chen, K. Shen, J.Y. Chen, X.D. Chen, Y.W. Li, Hollow-ZIF-templated formation of a ZnO@C–N–Co core–shell nanostructure for highly efficient pollutant photodegradation, *J. Mater. Chem. A* 5 (2017) 9937–9945.
- [50] X.G. Li, Q.L. Yao, Z.B. Li, H.B. Li, Q.L. Zhu, Z.H. Lu, Porphyrin frameworks-derived N-doped porous carbon-confined Ru for NH₃BH₃ methanolysis: the more pyridinic-N, the better, *J. Mater. Chem. A* 10 (2022) 326–336.
- [51] D.W. Gao, Z.L. Wang, C. Wang, H.L. Wang, Y. Chi, M.G. Wang, J.J. Zhang, C. Wu, Y. Gu, H. Wang, Z.K. Zhao, CrPd nanoparticles on NH₂-functionalized metal–organic framework as a synergistic catalyst for efficient hydrogen evolution from formic acid, *Chem. Eng. J.* 361 (2019) 953–959.
- [52] Q.J. Wang, N. Tsumori, M. Kitta, Q. Xu, Fast dehydrogenation of formic acid over palladium nanoparticles immobilized in nitrogen-doped hierarchically porous carbon, *ACS Catal.* 8 (2018) 12041–12045.
- [53] X.J. He, P.H. Ling, M.X. Yu, X.T. Wang, X.Y. Zhang, M.D. Zheng, Rice husk-derived porous carbons with high capacitance by ZnCl₂ activation for supercapacitors, *Electrochim. Acta* 105 (2013) 635–641.
- [54] J. Cheng, X. Gu, X. Sheng, P. Liu, H. Su, Exceptional size-dependent catalytic activity enhancement in the room-temperature hydrogen generation from formic acid over bimetallic nanoparticles supported by porous carbon, *J. Mater. Chem. A* 4 (2016) 1887–1894.
- [55] S. Kim, J. Park, J. Hwang, J. Lee, Effects of functional supports on efficiency and stability of atomically dispersed noble-metal electrocatalysts, *EnergyChem* 3 (2021), 100054.
- [56] W. Wang, X. Hong, Q. Yao, Z.-H. Lu, Bimetallic Ni–Pt nanoparticles immobilized on mesoporous N-doped carbon as a highly efficient catalyst for complete hydrogen evolution from hydrazine borane, *J. Mater. Chem. A* 8 (2020) 13694–13701.
- [57] Q.L. Yao, Z.H. Lu, Y.W. Yang, Y.Z. Chen, X.S. Chen, H.L. Jiang, Facile synthesis of graphene supported Ni–CeO_x nanocomposites for highly efficient catalysis in hydrolytic dehydrogenation of ammonia borane, *Nano Research* 11 (2018) 4412–4422.
- [58] Q. Wang, D. Astruc, State of the art and prospects in metal–organic framework (MOF)-based and MOF-derived nanocatalysis, *Chem. Rev.* 120 (2020) 1438–1511.
- [59] J.S. Meng, C.J. Niu, L.H. Xu, J.T. Li, X. Liu, X.P. Wang, Y.Z. Wu, X.M. Xu, W. Y. Chen, Q. Li, Z.Z. Zhu, D.Y. Zhao, L.Q. Mai, General oriented formation of carbon nanotubes from metal–organic frameworks, *J. Am. Chem. Soc.* 139 (2017) 8212–8221.
- [60] V. Mazumder, S.H. Sun, Oleylamine-mediated synthesis of Pd nanoparticles for catalytic formic acid oxidation, *J. Am. Chem. Soc.* 131 (2009) 4588–4589.
- [61] M.H. Shao, T. Yu, J.H. Odell, M.S. Jin, Y.N. Xia, Structural dependence of oxygen reduction reaction on palladium nanocrystals, *Chem. Commun.* 47 (2011) 6566–6568.
- [62] T. Jawhari, A. Roid, J. Casado, Raman spectroscopic characterization of some commercially available carbon black materials, *Carbon* 33 (1995) 1561–1565.
- [63] Q.J. Wang, L. Chen, Z. Liu, N. Tsumori, M. Kitta, Q. Xu, Phosphate-mediated immobilization of high-performance AuPd nanoparticles for dehydrogenation of formic acid at room temperature, *Adv. Funct. Mater.* 29 (2019), 1903341.
- [64] C. Wan, L. Zhou, S.M. Xu, B.Y. Jin, X. Ge, X. Qian, L.X. Xu, F.Q. Chen, X.L. Zhan, Y. R. Yang, D.G. Cheng, Defect engineered mesoporous graphitic carbon nitride modified with AgPd nanoparticles for enhanced photocatalytic hydrogen evolution from formic acid, *Chem. Eng. J.* 429 (2022), 132388.
- [65] Q.Y. Bi, J.D. Lin, Y.M. Liu, H.Y. He, F.Q. Huang, Y. Cao, Dehydrogenation of formic acid at room temperature: boosting palladium nanoparticle efficiency by coupling with pyridinic-nitrogen-doped carbon, *Angew. Chem. Int. Ed.* 55 (2016) 11849–11853.

- [66] L. Yang, L.T. Huang, Y.H. Yao, L.F. Jiao, In-situ construction of lattice-matching NiP₂/NiSe₂ heterointerfaces with electron redistribution for boosting overall water splitting, *Appl. Catal. B* 282 (2021), 119584.
- [67] K. Tedsree, C.W.A. Chan, S. Jones, Q. Cuan, W.K. Li, X.Q. Gong, S.C.E. Tsang, ¹³C NMR guides rational design of nanocatalysts via chemisorption evaluation in liquid phase, *Science* 332 (2011) 224–228.
- [68] Q.L. Zhu, N. Tsumori, Q. Xu, Sodium hydroxide-assisted growth of uniform Pd nanoparticles on nanoporous carbon MSC-30 for efficient and complete dehydrogenation of formic acid under ambient conditions, *Chem. Sci.* 5 (2014) 195–199.
- [69] M. Molina-Sabio, F. Rodríguez-Reinoso, F. Caturia, M.J. Sellés, Porosity in granular carbons activated with phosphoric acid, *Carbon* 33 (1995) 1105–1113.
- [70] C. Xie, D. Yan, H. Li, S.Q. Du, W. Chen, Y.Y. Wang, Y.Q. Zou, R. Chen, S.Y. Wang, Defect chemistry in heterogeneous catalysis: recognition, understanding, and utilization, *ACS Catal.* 10 (2020) 11082–11098.
- [71] F. Suárez-García, A. Martínez-Alonso, J.M.D. Tascón, Activated carbon fibers from Nomex by chemical activation with phosphoric acid, *Carbon* 42 (2004) 1419–1426.
- [72] J.G. Tu, H.P. Lei, Z.J. Yua, S.Q. Jiao, Ordered WO_{3-x} nanorods: facile synthesis and their electrochemical properties for aluminum-ion batteries, *Chem. Commun.* 54 (2018) 1343–1346.
- [73] Y. Cui, K. Xiao, N.M. Bedford, X.X. Lu, J. Yun, R. Amal, D.W. Wang, Refilling nitrogen to oxygen vacancies in ultrafine tungsten oxide clusters for superior lithium storage, *Adv. Energy Mater.* 9 (2019), 1902148.
- [74] I. Barlocco, S. Capelli, X.Y. Lu, S. Tumati, N. Dimitratos, A. Roldan, A. Villa, Role of defects in carbon materials during metal-free formic acid dehydrogenation, *Nanoscale* 12 (2020) 22768–22777.
- [75] R. Li, Z. Liu, Q.T. Trinh, Z. Miao, S. Chen, K. Qian, R.J. Wong, S. Xi, Y. Yan, A. Borgna, S. Liang, T. Wei, Y. Dai, P. Wang, Y. Tang, X. Yan, T.S. Choksi, W. Liu, Strong metal–support interaction for 2D materials: application in noble Metal/TiB₂ heterointerfaces and their enhanced catalytic performance for formic acid dehydrogenation, *Adv. Mater.* 33 (2021), 2101536.
- [76] X. Zhang, F.Y. Tian, X. Lan, Y.Q. Liu, W.W. Yang, J. Zhang, Y.S. Yu, Building P-doped MoS₂/g-C₃N₄ layered heterojunction with a dual-internal electric field for efficient photocatalytic sterilization, *Chem. Eng. J.* 429 (2022), 132588.
- [77] X. Zhang, F.Y. Tian, M.Y. Gao, W.W. Yang, Y.S. Yu, L-Cysteine capped Mo₂C/Zn_{0.67}Cd_{0.33}S heterojunction with intimate covalent bonds enables efficient and stable H₂-Releasing photocatalysis, *Chem. Eng. J.* 428 (2022), 132628.
- [78] X. Zhang, W.W. Yang, M.Y. Gao, H. Liu, K.F. Liu, Y.S. Yu, Room-temperature solid phase surface engineering of BiOI sheets stacking g-C₃N₄ boosts photocatalytic reduction of Cr(VI), *Green Energy Environ.* 7 (2022) 66–74.
- [79] T.T. Hou, Q.Q. Luo, Q. Li, H.L. Zu, P.X. Cui, S.W. Chen, Y. L, J.J. Chen, X.S. Zheng, W.K. Zhu, S.Q. Liang, J.L. Yang, L.B. Wang, Modulating oxygen coverage of Ti₃C₂T_x MXenes to boost catalytic activity for HCOOH dehydrogenation, *Nat. Commun.* 11 (2020) 4251.
- [80] M.C. Wen, K. Mori, Y. Kuwahara, H. Yamashita, Plasmonic Au@Pd nanoparticles supported on a basic metal–organic framework: synergic boosting of H₂ production from formic acid, *ACS Energy Lett.* 2 (2017) 1–7.